

Demonstration and characterization of ultrafast laser-inscribed mid-infrared waveguides in chalcogenide glass IG2

Citation for published version:

Butcher, HL, MacLachlan, DG, Lee, D, Thomson, RR & Weidmann, D 2018, 'Demonstration and characterization of ultrafast laser-inscribed mid-infrared waveguides in chalcogenide glass IG2', *Optics Express*, vol. 26, no. 8, pp. 10930-10943. <https://doi.org/10.1364/OE.26.010930>

Digital Object Identifier (DOI):

[10.1364/OE.26.010930](https://doi.org/10.1364/OE.26.010930)

Link:

[Link to publication record in Heriot-Watt Research Portal](#)

Document Version:

Publisher's PDF, also known as Version of record

Published In:

Optics Express

General rights

Copyright for the publications made accessible via Heriot-Watt Research Portal is retained by the author(s) and / or other copyright owners and it is a condition of accessing these publications that users recognise and abide by the legal requirements associated with these rights.

Take down policy

Heriot-Watt University has made every reasonable effort to ensure that the content in Heriot-Watt Research Portal complies with UK legislation. If you believe that the public display of this file breaches copyright please contact open.access@hw.ac.uk providing details, and we will remove access to the work immediately and investigate your claim.



Demonstration and characterization of ultrafast laser-inscribed mid-infrared waveguides in chalcogenide glass IG2

HELEN L. BUTCHER,¹ DAVID G. MACLACHLAN,² DAVID LEE,³ ROBERT R. THOMSON,² AND DAMIEN WEIDMANN^{1,*}

¹Space Science and Technology Department (RAL Space), STFC Rutherford Appleton Laboratory, Harwell Campus, Didcot, OX11 0QX, UK

²Scottish Universities Physics Alliance (SUPA), Institute of Photonics and Quantum Sciences, School of Engineering and Physical Sciences, David Brewster Building, Heriot Watt University, Edinburgh, EH14 4AS, UK

³Science and Technology Facilities Council, UK Astronomy Technology Centre, Blackford Hill, Edinburgh, EH9 3HJ, UK

*damiem.weidmann@stfc.ac.uk

Abstract: The first demonstration and characterization of ultrafast laser-inscribed mid-infrared (mid-IR) waveguides in $\text{Ge}_{33}\text{As}_{12}\text{Se}_{55}$ chalcogenide glass (IG2) is presented. From mode profile and throughput measurements, combined with modelling, the characteristics of the waveguides inscribed in IG2 are studied at 7.8 μm , and compared to those of waveguides inscribed in gallium lanthanum sulfide for reference. Two methods to estimate the local variation of refractive index induced by the inscription process are presented, which indicate a variation of ~ 0.010 to 0.015 across the inscription parameters investigated. This variation, together with a higher robustness of the material to inscription and large transparency covering the entire mid-IR spectral domain, suggest that IG2 has great potential for integrated optical applications in the mid-IR developed through the ultrafast laser inscription method.

Published by The Optical Society under the terms of the [Creative Commons Attribution 4.0 License](https://creativecommons.org/licenses/by/4.0/). Further distribution of this work must maintain attribution to the author(s) and the published article's title, journal citation, and DOI

OCIS codes: (130.3060) Infrared; (130.3130) Integrated optics materials; (140.5965) Semiconductor lasers, quantum cascade; (220.4610) Optical fabrication; (230.7370) Waveguides.

References and links

1. T. Schädle and B. Mizaikoff, "Mid-infrared waveguides: A perspective," *Appl. Spectrosc.* **70**(10), 1625–1638 (2016).
2. I. S. Glass, *Handbook of Infrared Astronomy* (Cambridge University, 1999).
3. H.-K. Hsiao, K. A. Winick, J. D. Monnier, and J.-P. Berger, "An infrared integrated optic astronomical beam combiner for stellar interferometry at 3–4 μm ," *Opt. Express* **17**(21), 18489–18500 (2009).
4. A. Arriola, S. Mukherjee, D. Choudhury, L. Labadie, and R. R. Thomson, "Ultrafast laser inscription of mid-IR directional couplers for stellar interferometry," *Opt. Lett.* **39**(16), 4820–4822 (2014).
5. J. Kasberger, T. Fromherz, A. Saeed, and B. Jakoby, "Miniaturized integrated evanescent field IR-absorption sensor: Design and experimental verification with deteriorated lubrication oil," *Vib. Spectrosc.* **56**, 129–135 (2011).
6. P. T. Lin, V. Singh, J. Hu, K. Richardson, J. D. Musgraves, I. Luzinov, J. Hensley, L. C. Kimerling, and A. Agarwal, "Chip-scale mid-infrared chemical sensors using air-clad pedestal silicon waveguides," *Lab Chip* **13**(11), 2161–2166 (2013).
7. V. M. Lavchiev and B. Jakoby, "Photonics in the mid-infrared: challenges in single-chip integration and absorption sensing," *IEEE J. Sel. Top. Quant.* **23**(2), 8200612 (2017).
8. R. Soref, "Toward silicon-based longwave integrated optoelectronics (LIO)," *Proc. SPIE* **6898**, 689809 (2008).
9. N. Hô, M. C. Phillips, H. Qiao, P. J. Allen, K. Krishnaswami, B. J. Riley, T. L. Myers, and N. C. Anheier, Jr., "Single-mode low-loss chalcogenide glass waveguides for the mid-infrared," *Opt. Lett.* **31**(12), 1860–1862 (2006).
10. A. Arriola, S. Gross, M. Ams, T. Gretzinger, D. Le Coq, R. P. Wang, H. Ebendorff-Heidepriem, J. Sanghera, S. Bayya, L. B. Shaw, M. Ireland, P. Tuthill, and M. J. Withford, "Mid-infrared astrophotonics: study of ultrafast laser induced index change in compatible materials," *Opt. Mater. Express* **7**(3), 698–711 (2017).

11. R. R. Thomson, R. J. Harris, T. A. Birks, G. Brown, J. Allington-Smith, and J. Bland-Hawthorn, "Ultrafast laser inscription of a 121-waveguide fan-out for astrophotonics," *Opt. Lett.* **37**(12), 2331–2333 (2012).
12. A. Ródenas, G. Martín, B. Arezki, N. Psaila, G. Jose, A. Jha, L. Labadie, P. Kern, A. Kar, and R. Thomson, "Three-dimensional mid-infrared photonic circuits in chalcogenide glass," *Opt. Lett.* **37**(3), 392–394 (2012).
13. Vitron IG2 datasheet, <http://www.vitron.de/english/IR-Glaeser/Daten-Infrarotglaeser.php>.
14. Optical constants of Vitron IG2, <https://refractiveindex.info/?shelf=glass&book=VITRON-IG&page=IG2>.
15. D. Lee, D. G. MacLachlan, H. L. Butcher, R. A. Brownsword, D. Weidmann, C. R. Cunningham, H. Schnetler, and R. R. Thomson, "Mid-infrared transmission gratings in chalcogenide glass manufactured using ultrafast laser inscription," *Proc. SPIE* **9912**, 91222X (2016).
16. H. L. Butcher, D. Lee, R. Brownsword, D. G. MacLachlan, R. R. Thomson, and D. Weidmann, "Ultrafast laser-inscribed mid-infrared transmission gratings in IG2: modelling and high-resolution spectral characterization," *Opt. Express* **25**(26), 33617–33628 (2017).
17. Gallium Lanthanum Sulphide (GLS) datasheet, <https://www.crystran.co.uk/optical-materials/gallium-lanthanum-sulphide-gls>.
18. D. G. MacLachlan, R. R. Thomson, C. R. Cunningham, and D. Lee, "Mid-infrared volume phase gratings manufactured using ultrafast laser inscription," *Opt. Mater. Express* **3**(10), 1616–1623 (2013).
19. M. Ams, G. D. Marshall, and M. J. Withford, "Study of the influence of femtosecond laser polarisation on direct writing of waveguides," *Opt. Express* **14**(26), 13158–13163 (2006).
20. R. R. Thomson, N. D. Psaila, H. T. Bookey, D. T. Reid, and A. K. Kar, "Controlling the cross-section of ultrafast laser inscribed optical waveguides," in *Femtosecond Laser Micromachining*, R. Osselame, G. Cerullo and R. Ramponi, ed. (Springer-Verlag, 2012).
21. K. Okamoto, *Fundamentals of Optical Waveguides*, (Elsevier, 2006).
22. M. H. Jericho, H. J. Kreuzer, M. Kanka, and R. Riesenberger, "Quantitative phase and refractive index measurements with point-source digital holographic measurement," *Appl. Opt.* **51**(10), 1503–1515 (2012).
23. P. Bastock, C. Craig, K. Khan, E. Weatherby, J. Yao, and D. W. Hewak, "Properties of gallium lanthanum sulphide glass," in *CLEO: 2015, OSA Technical Digest* (online) (Optical Society of America, 2015), paper STh1G.1.

1. Introduction

Infrared (IR) optical waveguides are a mature technology enabling integrated optics, with wide-ranging functions and applications across many industrial sectors [1]. This is particularly so in the near-IR part of the spectrum, where silica-based waveguides have enabled low-cost and rugged optical communications, to name only a leading example. Extending waveguide technologies towards longer wavelengths would widen the benefit of integrated optics. The mid-IR part of the electromagnetic spectrum (2–20 μm) is of particular interest as far as molecular optical sensing is concerned. Indeed, in this spectral region, by means of high resolution spectroscopy, molecules can be sensed with high specificity, as they exhibit unique fundamental ro-vibrational bands. Besides, in the mid-IR, two atmospheric windows, 3–5 μm and 8–12 μm , are available, in which spectral interference from water vapor is limited, which is advantageous in applications such as remote atmospheric sounding and astronomy [2].

Mid-IR waveguides are sought after to serve many fields. Drawing on knowledge from fiber telecommunications, components such as evanescent field couplers have been demonstrated that significantly reduce the dimensions of optical layouts compared to traditional free-space beamsplitters. These couplers have been demonstrated in astrophotonics applications, with waveguide arrays used for beam combination in stellar interferometry [3]. [4]. Evanescent field sensing of refractive index using waveguide-integrated structures has been exploited for numerous lab-on-a-chip sensing devices [5,6]. These devices, when extended to the mid-IR, draw the benefits of improved specificity and sensitivity for spectroscopic applications [7].

Planar waveguide technology in the mid-IR has mainly focused on silicon photonics to date, exploiting conventional micro-electronics foundry techniques for high-quantity wafer-scale production [8]. These methods typically require numerous mask-etch and mask-grow steps to create structures suitable for waveguiding, and as such are high-risk, expensive processes for initial device study. Alternative materials for the mid-IR spectral region include chalcogenides, which can be grown or deposited on host substrates to form planar layers, and subsequently etched to define waveguide structures. These typically have low propagation

losses, < 1 dB/cm [9], but again suffer from costly, large-scale fabrication processes that are prohibitive for optimized device development. Neither method can be used to define waveguide structures out of the grown-material plane.

Ultrafast laser inscription (ULI) provides a highly cost-effective and convenient method of inscribing waveguides structures in mid-IR photonic materials [10]. Not only does it allow rapid prototyping in a wide range of transmissive mid-IR materials, but it also opens up a third manufacturing dimension that can be exploited for novel photonic structures, for instance in developing photonic lanterns [11]. Single devices can be fabricated quickly for rapid design-fabricate-test optimization. ULI waveguides typically have low refractive index contrast, $\Delta n < 0.01$ [10], which is highly dependent on the material properties, inscription regime and fabrication parameters used. This limits the bend radii that can be employed in complex low-loss waveguide geometries such as evanescent field couplers.

Waveguide inscription in chalcogenide materials has previously been demonstrated in commercial and research glass compositions, including single-mode waveguides in gallium lanthanum sulfide (GLS) at $3.39\text{ }\mu\text{m}$, and single- and multi-mode waveguides in research composition $75\text{GeS}_2\text{-}15\text{Ga}_2\text{S}_3\text{-}4\text{CsI-}2\text{Sb}_2\text{S}_3\text{-}4\text{SnS}$ (GCIS) at $10.6\text{ }\mu\text{m}$ [12]. IG2 ($\text{Ge}_{33}\text{As}_{12}\text{Se}_{55}$) is a commercial, well-established, chalcogenide composition commonly used in mid-IR applications [13]. It transmits over the entire $1\text{--}12\text{ }\mu\text{m}$ spectral region [14], and as such is an ideal candidate for the development of waveguide structures in the mid-IR. ULI has been proven in IG2 photonic glass for the inscription of mid-IR volume gratings, and was shown to exhibit larger refractive index modification than GLS under similar inscription conditions [15,16].

The purpose of this study is to demonstrate and characterize the ULI fabrication parameter space for waveguides in IG2, as well as in GLS for comparison, and to interpret these parameters within the context of waveguide modeling. The comparison of performance between waveguides inscribed in the two glasses at $7.8\text{ }\mu\text{m}$ highlights the benefits of IG2 for ULI waveguide structures. Firstly, the fabrication and characterization methods for single- and multi-mode straight waveguides are described. Following this, a comparison of fabrication parameters for each material is presented. Finally, two methods of determining estimates of the refractive index modification (Δn) caused by ULI are derived, based on analysis of the output mode profiles of the waveguides and comparison to modelled expectations, with which full quantitative waveguide modelling is carried out.

2. Waveguide fabrication

Waveguides in IG2 [13] and GLS [17], both commercial compositions, were fabricated using a ULI system previously described elsewhere [18]. In short, the source is a pulsed fiber laser (Menlo BlueCut) that operates at 1030 nm and produces 355 fs pulses at 500 kHz repetition rate. The polarization state is circular [19]. A microscope objective with numerical aperture of 0.55 was used to create a beam waist of approximately $1\text{ }\mu\text{m}$ within the chalcogenide substrate. The substrate was then moved within the beam focus in three-dimensions using an air bearing stage system (Aerotech ABL1000), to create the modified refractive index paths required for waveguiding.

All inscribed waveguides were 20 mm long, and inscribed in chips $20 \times 10 \times 1\text{ mm}^3$, which were polished on the $10 \times 1\text{ mm}^2$ faces prior to inscription. Whilst IG2 waveguides were inscribed to the edges of the chip without any issues, this was found to be impossible with GLS owing to facet material damage; previous results required post-inscription facet polishing [4]. As a result, GLS waveguides were inscribed to within $50\text{ }\mu\text{m}$ of the chip edges, with acknowledgment of the small amount of addition coupling loss that will occur for this propagation in the bulk material. Waveguides were inscribed $\sim 150\text{ }\mu\text{m}$ deep in IG2 and $\sim 200\text{ }\mu\text{m}$ deep in GLS. The multi-scan inscription method was used; multiple narrow lines of modified refractive index were inscribed close to one another to create a modified material

region wide enough for single- or multi-mode guiding. The $1/e^2$ spot size overlap was approximately 70%, corresponding to horizontal scan spacing of $0.3\ \mu\text{m}$.

Waveguide performance was characterized by observing both the intensity mode profile and the optical power at the output of the waveguide. Fabrication parameters were chosen to provide a range of single- and multi-mode waveguides for a parametric study; these were informed by extensive prior study of waveguide fabrication in GLS [4,12], and initial test waveguide chips to determine suitable inscription parameters for each material. Two fabrication parameters were varied: the inscribed waveguide horizontal dimension; and the pulse energy used to create the inscribed region. Varying the pulse energy affects both the refractive index modification achieved, and also the vertical dimension of the waveguide due to increased fluence in the focal region. The fabrication parameter range used to produce waveguides in each chalcogenide is given in Table 1. Each waveguide was made up of a number of horizontal and vertical scans; each horizontal scan was spaced $0.3\ \mu\text{m}$ apart as described above, and, in GLS only, vertical scans were spaced to create an approximately square waveguide cross-section. Waveguides in GLS with multiple vertical layers required lower pulse energy per layer to achieve the same refractive index modification as waveguides that consist of a single vertical layer, due to the overlap of inscribed regions.

Table 1. Waveguide fabrication parameter range

Material	IG2	GLS
Inscription speed	10 mm/s	8 mm/s
Pulse energy	10.44–16.62 nJ, for single layer inscription	48.7–60.9 nJ, single layer 22.6–39.2 nJ, two layer 22.6–33.9 nJ, three layer
Number of horizontal scans	50–78, for waveguide cross-section $15\text{--}23.4\ \mu\text{m}$	60–120, for waveguide cross-section $18\text{--}36\ \mu\text{m}$
Number of vertical scans	1 for waveguide vertical cross-section $\approx 20\ \mu\text{m}$	1 for waveguides $\approx 20\ \mu\text{m}$ 2 for waveguides $24\text{--}30\ \mu\text{m}$ 3 for waveguides $\approx 36\ \mu\text{m}$
Number of waveguides	77	32
Bulk refractive index at $7.85\ \mu\text{m}$	$n = 2.5032$ [14]	$n \approx 2.34$ [17]

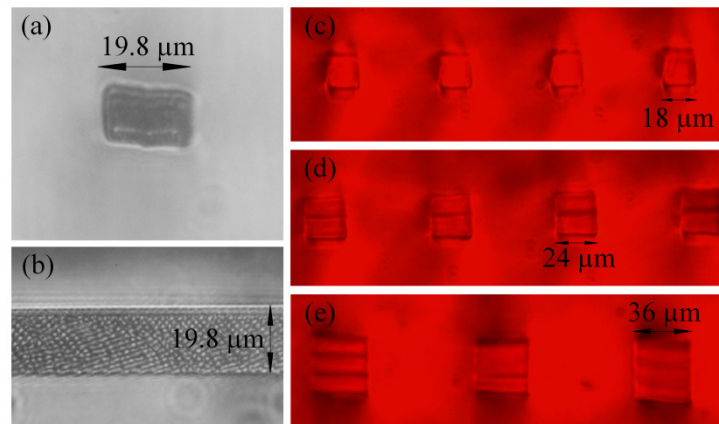


Fig. 1. Images of fabricated waveguides. (a) IG2 waveguide facet, (b) IG2 waveguide from surface, (c)–(e) GLS waveguides, showing single, double and triple inscription layers, respectively.

Waveguides were separated by a minimum of $100\ \mu\text{m}$ in IG2, and $60\ \mu\text{m}$ in GLS. Images of the IG2 and GLS waveguides were obtained using a visible microscope and are shown in Fig. 1. The facet and IG2 surface images were obtained using a Leitz Ergolux microscope and standard DSLR camera, with the camera IR filter removed to obtain images of IG2. The GLS

surface image was obtained using Zeiss Stemi 2000-CS microscope. Figure 1(b) shows that the IG2 waveguides exhibit some sub-wavelength structuring, which is thought to result from the multiscan technique described above. The overlapping scan spacing of $0.3\ \mu\text{m}$ and $1\ \mu\text{m}$ inscription beam waist will contribute to this structuring along the length of the waveguide.

3. Waveguide characterization system

The waveguides were characterized at $7.85\ \mu\text{m}$, using a pulsed quantum cascade laser (QCL) (Alpes Lasers SA) mounted in a Cascade Technologies LM01 housing (with associated CM01 controller). The laser was operated with a forward voltage of 12 V at 15°C , outputting 50 ns pulses at a repetition rate of 400 kHz. Use of a pulsed laser system minimized the risk of damage to the QCL by reflection from the waveguide chip facet, allowing characterization of waveguides inscribed perpendicular to the waveguide chip facet and thus simplifying waveguide alignment.

Figure 2 shows a schematic of the characterization arrangement. The laser output was collimated using the integrated lens within the LM01 housing. Lenses L_1 and L_2 were used in a telescope arrangement to expand the beam waist to 1.5 mm; this was the optimum beam waist required to obtain a $1/e^2$ beam waist of approximately $10\ \mu\text{m}$ at the waveguide input facet using objective MO_1 . Objective MO_2 was identical to MO_1 , and was used to image the waveguide output on to the camera (Electrophysics PV320) or power meter (Ophir 3A) at position 'A'; position 'A' is the image plane in which the image of the facet is produced. MO_1 was static; both the waveguide chip and MO_2 were positioned using precision alignment stages (Newport M-SDS-40-XYZ and Thorlabs MBT616D/M, respectively) to optimize coupling to the waveguides.

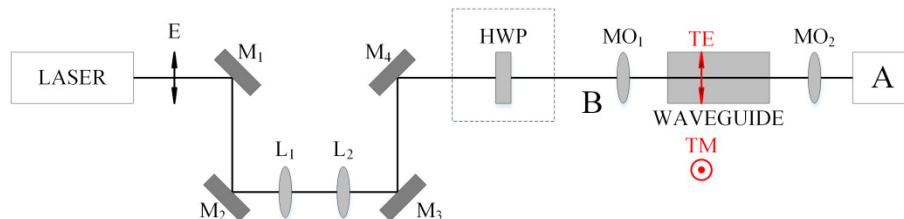


Fig. 2. Schematic of characterization equipment used to interrogate waveguides, shown from above. Mirrors M_1 – M_4 were used for beam steering. Lenses L_1 and L_2 were used in a telescope arrangement to expand the laser beam. Objectives MO_1 and MO_2 were used to couple into and out of the waveguide, with measurement made using a camera or power meter at position A. The polarization state of the incident beam 'E' on the waveguide facet was controlled by inserting or removing the half-wave plate (HWP), to interrogate the polarized waveguide modes 'TE' and 'TM'.

Polarization of the characterization beam was controlled by use of a half-wave plate (HWP) before MO_1 . The laser output is polarized in the plane parallel to the table surface, along direction 'E', such that the TE waveguide modes can be interrogated directly, see red annotation on Fig. 2. Characterization of the TM modes required use of the HWP to rotate the polarization state.

The camera was used to collect output beam profile images; these were processed using the Gauss2D surface fitting function in OriginPro data analysis and graphing software, to obtain $1/e^2$ beam waist and mode field diameter (MFD) values of the imaged output profile. The magnification of the system (the ratio of the distance between the waveguide output facet and MO_2 , and the distance between MO_2 and the image plane position 'A') was used to deduce the MFD at the waveguide output facet.

The power meter was used to obtain the throughput of the characterization system, to estimate the waveguide propagation losses. The waveguide output power could not be measured directly at the output facet due to the fast Gaussian beam expansion in the near-field (small output beam waist), and the large physical dimensions of the precision stage

system used to align the waveguide. The optical power and background level was measured with the detector at position 'B', prior to MO_1 , and at position 'A', after MO_2 . To estimate the propagation losses in the waveguide, contributions from other known sources of loss were calculated and are accounted for in all quoted values throughout this manuscript. These included: Fresnel reflections at the waveguide facet (GLS: $T = 0.723$ for $n \approx 2.34$ @ $7.85 \mu\text{m}$ [17]; IG2: $T = 0.673$ for $n = 2.5032$ @ $7.85 \mu\text{m}$ [14]); numerical aperture (NA) mismatch between objective MO_1 ($NA = 0.25$) and the waveguide input facet ($NA = 0.22$, typical), $T = 0.774$; and estimated losses due to the imperfect AR coating on four objective surfaces ($\sim 1\%$ loss per surface, $T = 0.961$). In total, this implies that without taking into account intrinsic waveguide transmission losses, the maximum waveguide throughput is $T = 0.537$ for GLS, and 0.501 for IG2; these values are used to calculate normalized waveguide throughput values in the remainder of this document. More rigorous coupling coefficient analysis would provide a better estimate of the input and output coupling losses, but these will be slightly different for each individual waveguide tested, assuming the characterization input beam dimensions remain constant and each waveguide in the parameter space has different facet dimensions and Δn . Assuming these losses form only a small proportion of the total overall throughput loss, and are in part considered by the NA mismatch outlined above, these small variations in coupling losses are neglected in this exercise.

4. Experimental results and modelling

4.1 Waveguide output profiles

The fundamental mode profile of all waveguides was characterized; example mode profiles for IG2 and GLS are shown in Figs. 3(a) and 3(b), respectively, as well as the residual from the 2D elliptical Gaussian mode fit in Figs. 3(c) and 3(d).

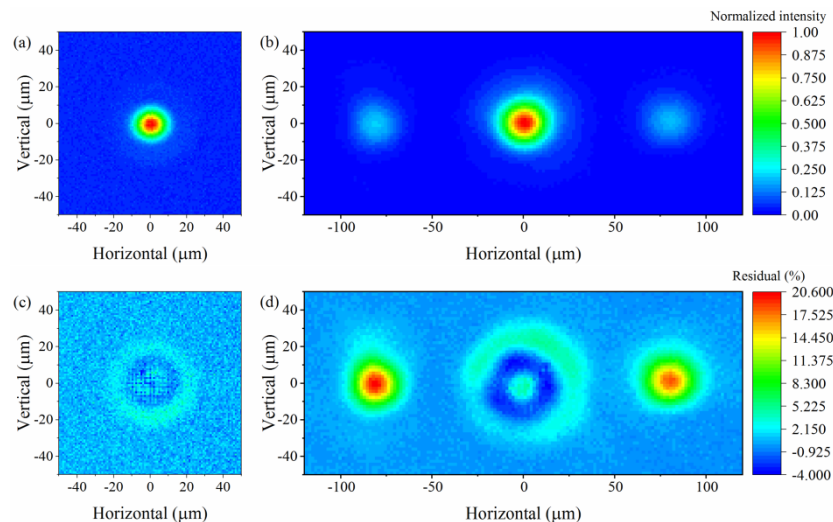


Fig. 3. Fundamental normalized intensity output mode profiles for (a) IG2 and (b) GLS, and residuals from fit of 2-dimensional elliptical Gaussian surface to data, for (c) IG2 and (d) GLS. The GLS profile was measured in the TM polarization state, had a horizontal cross-section of $20 \mu\text{m}$ and was inscribed with a pulse energy of 58.2 nJ . The IG2 profile was measured in the TE polarization state, had a horizontal cross-section of $19.6 \mu\text{m}$ and was inscribed with a pulse energy of 12.44 nJ .

For IG2, a Gaussian single waveguide output profile was observed, as expected for a waveguide spacing of $100 \mu\text{m}$. In GLS, the $60 \mu\text{m}$ spacing between waveguides was not large enough to stop evanescent coupling between adjacent waveguides. The less intense spots observed on either side of the main waveguide lobe are evidence that light is coupled into

adjacent waveguides. The IG2 waveguides were fabricated after the GLS waveguides, and the waveguide separation increased for IG2 to prevent coupling between adjacent waveguides. Modelling of these waveguides is described in more detail later in this manuscript.

In addition to the fundamental mode of the waveguide, higher order modes were observed at the output of a subset of both IG2 and GLS waveguides. Coupling to higher order modes was achieved by misaligning the waveguide from the fundamental mode, and optimizing coupling into a dual-lobe output mode. Only the second higher order mode was observed. In both cases, these modes were observed only for larger cross-section waveguides with larger inscription pulse energies (assumed to produce larger Δn). For IG2, a large subset of waveguides exhibited higher order mode behavior, for horizontal cross-sections from 19.8 to 23.4 μm with specific pulse energies. For GLS, higher order modes were only observed for waveguides with 36 μm cross-section, written at a slower inscription speed (4 mm/s). Example second order mode profiles are shown in Fig. 4. Using modelling, the fact that higher order modes can be supported will be used to deduce estimates of the Δn in section 4.2.

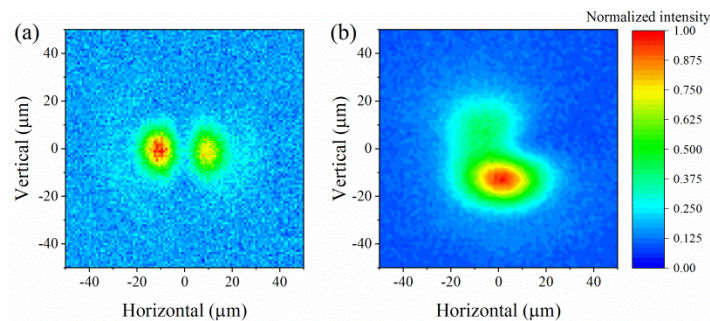


Fig. 4. Higher order waveguide output mode profiles. (a) IG2, measured mode was the TE_{21} mode, for the waveguide inscribed with 23.4 μm horizontal cross-section, and 14 nJ pulse energy. (b). GLS, measured mode was the TM_{21} mode, for the waveguide inscribed with 36 μm horizontal cross-section, 34.63 nJ pulse energy, and 4 mm inscription speed.

4.2 Mode field diameter study

The MFD of the measured fundamental mode of each waveguide was calculated from the fit to the data, in both horizontal and vertical dimensions, as described above. The theoretical relationship between MFD, core dimensions and refractive index modification (Δn) is well known, and is described in detail in the literature [20]. Comparison of the measured and modelled MFD for varying waveguide core dimensions should give an estimate of Δn achieved on inscription. Measured fundamental mode horizontal MFD was plotted against changing inscribed waveguide horizontal cross-section for each inscription pulse energy, points in Fig. 5, to observe the relationship between these experimental parameters. In addition, modelling of the MFD expected for discrete waveguide core dimensions and Δn was carried out using FIMMWAVE mode solving software. For the model, the waveguide facet dimensions were kept square.

The comparison between measured and modelled IG2 data in Fig. 5 shows that the fabricated Δn range covers 0.008–0.02, for pulse energies 10.44 nJ–16.62 nJ. In general, a trend of increasing Δn with increasing pulse energy is implied within this fabrication parameter space, this is shown in Fig. 6(a). The range of Δn for each pulse energy is also shown, and generally falls within $\Delta n \pm 0.002$.

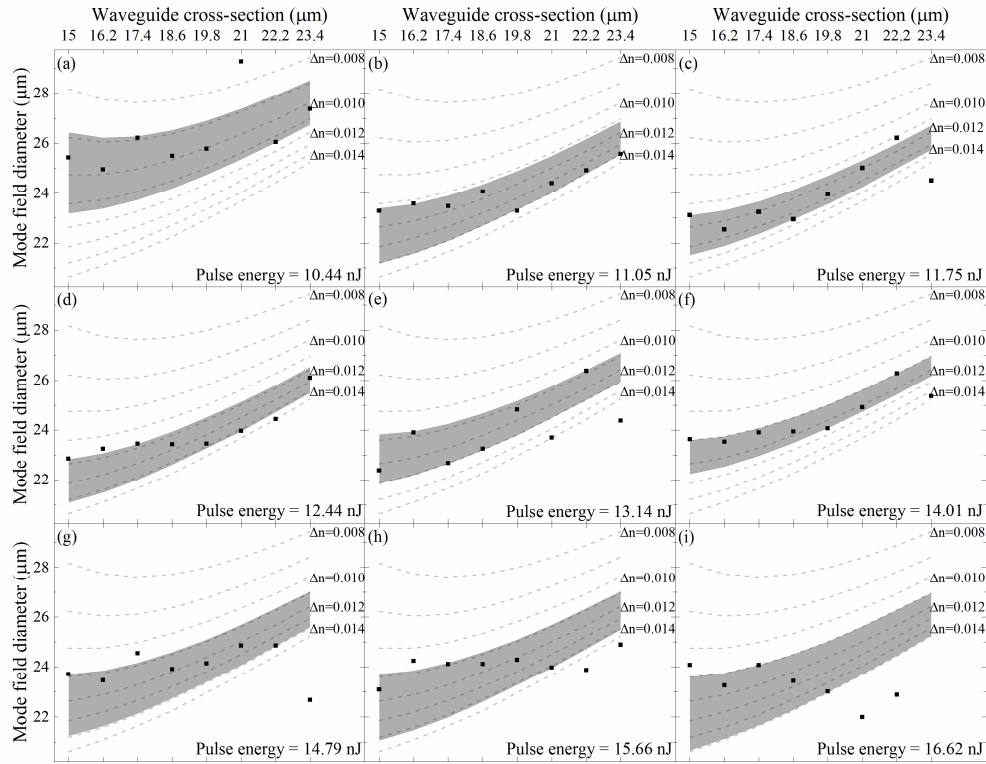


Fig. 5. Measured (points) and modeled (contour) horizontal MFD as a function of inscribed waveguide horizontal cross-section and modeled Δn , for individual pulse energies increasing across (a)–(i). All data presented was measured in the TE polarization state. Shaded regions define the approximate range of Δn for measured waveguides, with the exception of some outliers. All plots are on the same scale.

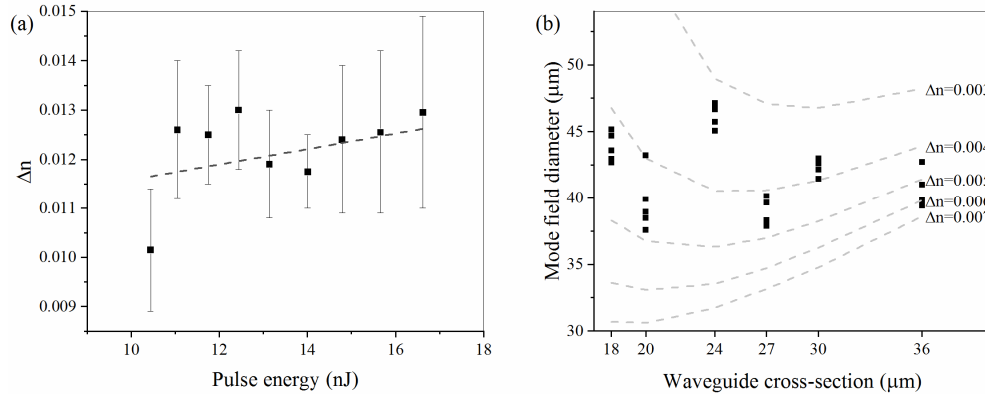


Fig. 6. (a) Increasing Δn with inscription pulse energy for IG2. Data points are median for each corresponding shaded region in Fig. 5, with error bars defining the full range. Dashed line is unweighted linear fit to data. (b) Relationship between horizontal MFD and horizontal waveguide cross-section for GLS.

Figure 5 and Fig. 6(a) show that the measured MFD, and therefore implied Δn is highly variable, and thus any observed correlation has high associated errors. These are due to a number of fabrication and model contributions, including manufacturing and measurement repeatability. For five nominally identical waveguides, the MFD was observed to vary by $\pm 1.5\%$, or $\pm 0.33 \mu\text{m}$ for a nominal $22 \mu\text{m}$ MFD waveguide. This includes errors from

fabrication (including $\pm 2\%$ variation of laser pulse energy during inscription, and $\pm 0.2 \mu\text{m}$ air bearing stage return error), and also measurement repeatability error of $\pm 0.6\%$ ($0.15 \mu\text{m}$ for a nominal waveguide with $25 \mu\text{m}$ measured MFD). In addition, all values include error from the MFD fitting procedure. This is small in comparison, at typically $0.03 \mu\text{m}$ for a purely single-mode waveguide. The full range of waveguides has MFD covering $22\text{--}29 \mu\text{m}$, and so each waveguide's total error covers more than 10% of the parameter space.

In addition, there will be some error associated with the model definition. The model assumes Δn is consistent throughout the volume of the modified region, which may not be the case in reality. The model also assumes a square waveguide cross-section, which for IG2 is clearly not the case, as in Fig. 1(a). However, each fabricated waveguide has different horizontal cross-section, and also different pulse energy which leads to different vertical cross-section. The vertical dimension variation has not been taken into consideration to simplify the model, on the grounds that the study employs only the horizontal MFD dimension.

Finally, the measured MFD is a measurement of the combination of the interaction between the input Gaussian beam to the waveguide and all of the excited modes of the waveguide structure. Thus for waveguides that support higher order modes, the 'fundamental' MFD measurement may also contain some contribution from the higher order modes, and the effect of an elliptical Gaussian laser beam. When comparing the residuals of the Gaussian fit for the two IG2 waveguides presented above, the residual range of the fundamental mode profile for the purely single-mode waveguide is approx. 1.7 times smaller than that of the residual of the fundamental mode of the waveguide that can support the higher order mode. In contrast, the modelled MFD is just the size of the supported mode within the waveguide structure, and does not contain any of these additional contributions. The outlying data points in Fig. 5, which particularly seem to occur for larger horizontal cross-section, large pulse energy waveguides in Figs. 5(e)–5(i), correspond to the waveguides that are observed to support higher order modes.

The MFD comparison for GLS is shown in Fig. 6(b). The pulse energy is different for each waveguide, and so a pulse energy trend similar to that identified for IG2 cannot be inferred. For GLS, the waveguide cross-sections were made square during the fabrication procedure, via control of the pulse energy and number of inscription layers, and as such a model with square waveguide dimensions was employed. The modelled data and larger than expected measured MFD implies that the refractive index modification of inscribed waveguides is lower than that anticipated [12], between $\Delta n = 0.003\text{--}0.006$. The close proximity of the waveguides and observed coupling between them will have an effect on the observed MFD of the waveguide. In addition, the presence of adjacent waveguide outputs on the mode profile will affect the Gaussian fitting procedure used to calculate MFD in the horizontal direction, as shown in Figs. 3(c) and 3(d). The residual range on fitting of the IG2 profile is $+0.0408/-0.0290$, while the residual range for GLS is larger, $+0.0441/-0.0361$.

4.3 Higher order mode cut-on: an alternative method to determine Δn

Whilst the study of the MFD dependence has given some insight into the achievable Δn produced by ULI, large uncertainties in the estimates call for an alternate estimation method. Higher-order mode cut-on can be used as a robust estimator of Δn . For a given Δn , higher-order modes will only be supported in a waveguide with sufficiently large core dimensions, which acts as a Δn threshold discriminator [21]. FIMMWAVE was used to calculate the effective index of the higher-order TE_{21} and TM_{21} modes in IG2 and GLS, respectively, for varying square waveguide dimensions and inscribed Δn . The higher order mode is deemed to be 'supported' only if the effective index of the higher order mode is greater than the refractive index of the unmodified bulk material (equivalent to the 'cladding' refractive index in optical fiber). Figure 7 shows the modelled data.

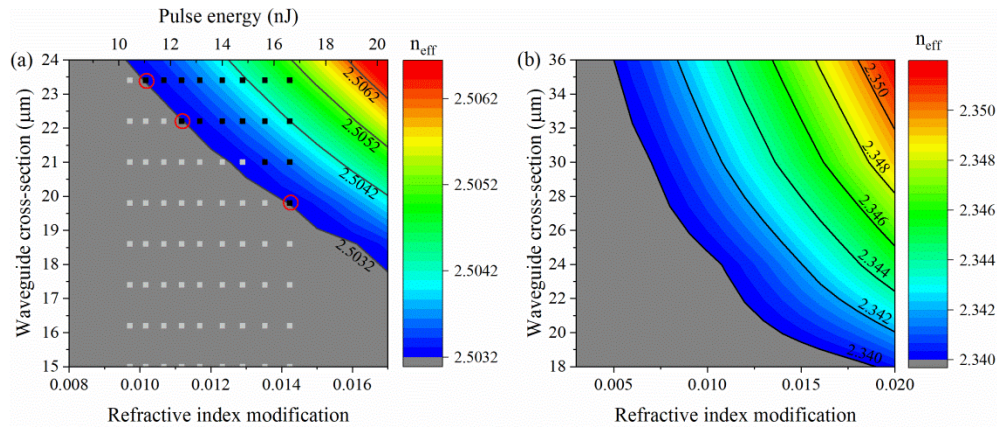


Fig. 7. Higher order mode cut-on for (a) IG2 and (b) GLS waveguides. Contours indicate the effective index of the higher order mode; the colored region indicates where the mode is supported ($n_{\text{eff}} > n_{\text{clad}}$). The points on the IG2 plot indicate waveguides fabricated with specific core dimensions and pulse energies (top axis). A black point indicates where the TE_{21} mode was observed at the output, while a grey point indicates the TE_{21} mode was not observed.

Higher-order mode cut on in IG2 is shown in Fig. 7(a). The TE_{21} mode was modelled to match the measured output mode profiles. The colored region shows waveguide parameters for which the mode is supported and can propagate, and the grey region indicates where the mode does not propagate. The overlaid data points indicate the experimental waveguide behavior, as a function of inscription pulse energy. Black points indicate that the higher order mode was observed at the waveguide output, while grey points indicate that only the fundamental mode was observed.

A subset of this data was used to infer the relationship between inscription pulse energy and Δn . The three data points chosen were the first for which higher order mode cut-on was observed for a specific horizontal waveguide cross-section. These are highlighted in red in Fig. 7(a). A further data point, at 21 μm cross-section, $\Delta n \approx 0.013$, should exhibit higher order mode behavior, but this was not observed during the measurement procedure, and it was disregarded as an outlier, impeded by manufacturing repeatability errors.

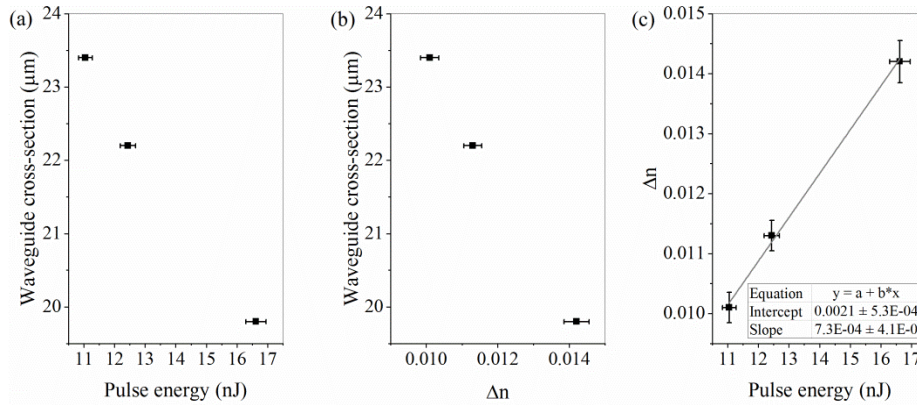


Fig. 8. Calculation of relationship between inscription pulse energy and refractive index modification. (a) Waveguide horizontal cross-section vs. inscription pulse energy. (b) Waveguide horizontal cross-section vs. modeled refractive index modification. (c) Linear fit between measured pulse energy and modelled refractive index modification, indicating the refractive index modification achieved on inscription.

The three waveguides are characterized in terms of horizontal waveguide cross-section versus pulse energy from the manufacturing parameters, shown in Fig. 8(a). Besides, the model allows the relationship between waveguide cross-section and refractive index modification to be determined, as shown in Fig. 8(b). By equating the waveguide cross-section values, the relationship between inscription pulse energy and refractive index modification can be inferred; this is shown in Fig. 8(c). Assuming a localized linear relationship between these parameters, the linear fit can be obtained that is then used to determine the axis scale relationship between pulse energy and refractive index modification, resulting in Fig. 7(a).

Use of this technique results in an estimate of the range of refractive index modification achieved as 0.0097–0.0142 over the range of 10.44–16.62 nJ pulse energy. The error in the refractive index modification estimated using this technique, by considering the half-distance between two adjacent data points, varied between ± 0.00022 to ± 0.00035 across the range. This value is determined by the limitations of the experimental points chosen; a further fabrication step to increase the number of different pulse energies would improve the precision of this value.

The waveguide horizontal cross-section is thought to be correct to within the return accuracy of the air-bearing stage system; this is the key factor that controls the overlap of the inscribed lines, and thus the refractive index modification across the waveguide profile. The accuracy of the system is quoted by the manufacturer as $\pm 0.2 \mu\text{m}$, implying a potential error in the waveguide cross-section of ± 1.3 to 0.5% for our 15–36 μm waveguides, respectively. These errors are too small to include in the data plots above, and are minimal compared to other errors. The inscription pulse energy was observed to vary by up to $\pm 2\%$ during waveguide inscription; this is included on the plots in Fig. 8.

The modeled refractive index modification contours show a non-linear relationship between refractive index modification and horizontal waveguide cross-section along the cut-on refractive index modification line (2.5032 contour). This is also highlighted in the non-zero crossing point of the linear relation between pulse energy and refractive index modification, with the calculated intercept at $\Delta n = 0.0021$. A non-linear fit between the two parameters would allow greater accuracy in the fit, however, with the limited data points available for the demonstration, such an exercise would not provide better understanding of the fabrication parameters at this time. This method appears promising and a larger data set should be used in the future to determine with more confidence the dependence of Δn on inscription pulse energy.

There is good agreement between the refractive index modification range achieved for IG2 using both the single-mode mode field diameter approach and the higher-order mode cut-on approach, with the higher order mode approach having calculated errors three times smaller. This implies that the simpler higher-order mode cut-on approach is a realistic indicator of the refractive index modification achieved for ULI in IG2, and more generally could be applied across all ULI waveguides for a well-designed parameter space. In the mid-infrared spectral region, direct measurement of the Δn by traditional methods, such as quantitative phase microscopy [22] or near-field refractive methods [20], is inhibited by the requirement for suitable transmissive refractive index-matching liquids with high n at these wavelengths. Demonstration of these robust methods for estimate of Δn is therefore significant for the development of mid-infrared ULI waveguides in general.

Figure 7(b) shows the FIMMWAVE model for a square GLS waveguide. Similarly to IG2, the higher order TM_{21} mode propagates in the waveguide if its cross-section and refractive index modification place it in the colored region of the plot. Conversely, the mode does not propagate if the cross-section and index modification place it in the grey region of the plot. The TM_{21} mode was modelled for each fabricated waveguide dimension, and Δn increased until the higher-order mode was supported for each dimension. In the experiment, higher order modes were observed only for 36 x 36 μm^2 cross-section GLS waveguides, while

all other smaller cross-sections allowed only fundamental mode propagation. This leads to an estimate that GLS waveguides have Δn less than 0.007, with 36 μm horizontal cross-section waveguides having Δn between 0.005 and 0.007. This is broadly consistent with the mode field diameter analysis above.

4.4 Modelled mode profiles

The mode field diameter and higher order mode cut-on studies above have allowed an estimation of the refractive index contrast induced by ULI inscription. There is good agreement between the two methods investigated, though the higher mode cut-on approach is deemed more accurate. Knowing Δn , the mode profiles outputted by the IG2 waveguides can be modelled and compared to the experimental ones presented in section 4.1.

Measured and modelled output profiles for IG2 are shown in Fig. 9. Both fundamental and higher-order mode behavior has been considered. Horizontal MFD of the single-mode profile was measured as 26.96 μm . The corresponding modelled profile, with cross-section 19.8 μm square and inscribed with pulse energy 12.44 nJ, corresponding to $\Delta n = 0.0113$ from the higher-order mode plot Fig. 7(a), yielded an MFD = 25.80 μm . Agreement between the model and the measured MFD is within 5%, indicating that the estimate of Δn by a combination of MFD measurement and higher order mode cut-on provides robust values. Higher order mode profiles are provided for qualitative comparison. The measured higher-order mode profile is obtained by misaligning the waveguide with respect to the incoming beam, hence the difference in observed power in the two lobes of the higher-order mode. The modelled higher-order mode is the solution to Maxwell's equations governing the behavior of the waveguide with square cross-section 23.4 μm and $\Delta n = 0.0125$, for pulse energy 14.01 nJ, from Fig. 7(a), and therefore does not show preferential coupling to either lobe.

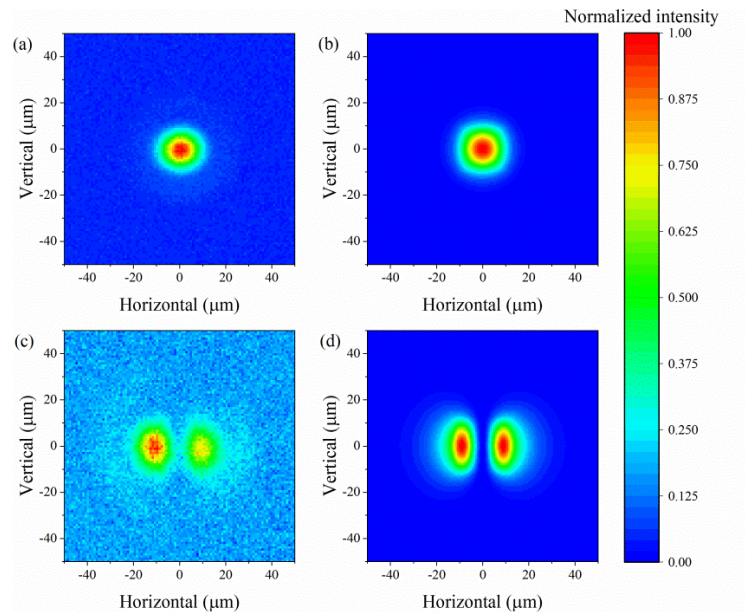


Fig. 9. Measured and modelled mode profiles in IG2. (a) Measured and (b) modelled fundamental mode profile of a single-mode IG2 waveguide, fabricated with 19.8 μm horizontal cross-section and 12.44 nJ pulse energy. Δn for the model was 0.0113, from Fig. 7(a). (c) Measured and (d) modelled mode profile of the TE_{21} mode of a multimode IG2 waveguide, fabricated with 23.4 μm inscribed horizontal cross-section and 14.0 nJ pulse energy. Δn for the model was 0.0125, from Fig. 7(a).

Similarly, measured and modelled mode profiles were observed for a single-mode GLS waveguide. In this case, a more complex model was constructed to consider the degree of

coupling between adjacent waveguides. Waveguides with 20 μm square cross-section were separated by 60 μm of unmodified material ($n \approx 2.34$). Δn was estimated to be 0.0047, from Fig. 7(b), and was the same for all three waveguides. Measured and modelled mode profiles are shown in Fig. 10.

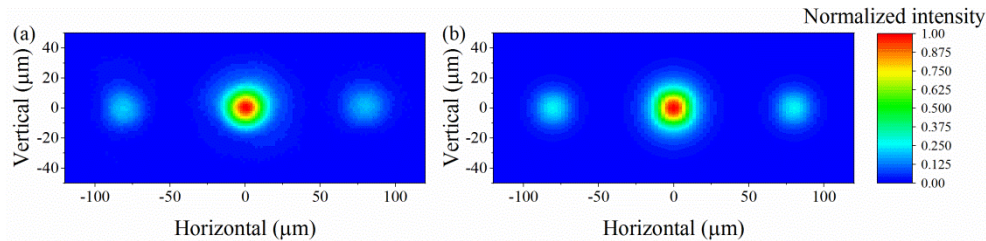


Fig. 10. (a) Measured and (b) modelled output profile for a single-mode GLS waveguide. These plots show coupling to adjacent waveguides inscribed 60 μm to each side of the center waveguide. Model parameters were: $\Delta n = 0.0047$; waveguide cross-section = 20 μm ; waveguide separation = 60 μm .

The horizontal MFD of the modelled waveguide was 37.48 μm , while the experimental MFD was 38.44 μm . The intensity of power coupled to the side waveguide was 25.1% in the model, and 21.7% in the measured mode profile. Once again, this good agreement between the measurement and model indicates robust knowledge of the refractive index modification achieved using ULI. Small variations in measured and modelled MFD and coupled waveguide output intensity are likely due to a combination of fabrication inconsistencies between adjacent waveguides, measurement error and accuracy of initial parameters chosen for the models.

4.5 Waveguide propagation losses

The normalized waveguide throughput of the single-mode waveguides was measured, as described above, by normalization to the maximum waveguide throughput calculated by considering known sources of loss within the measurement system (section 3). For IG2, typical normalized waveguide throughput was 55–60%. For GLS, typical normalized throughput was 5–5.5%. Assuming the normalized waveguide throughput losses consist wholly of propagation loss, which is justified through the consideration of other loss contributions in section 3, this implies propagation losses of approx. 1–1.5 dB/cm in IG2, and approx. 6.4 dB/cm in GLS. For IG2, these values agree well with quoted values for single-mode ULI waveguides in other materials [4].

For GLS, the propagation loss is much higher than previously observed [4]. Coupling of power to the adjacent waveguides in GLS will make the structure much lossier than the IG2 structure. Due to the geometry of the GLS structure, it is not possible to measure the throughput of the central waveguide alone, so measured throughput is a combination of all coupled waveguides. Propagation through unmodified material and lateral coupling between waveguides will increase propagation losses of the device; these losses go some way to explaining the relatively lower power observed for the GLS structure. In addition, cut-off for the 20 mm thick GLS material used was measured using a Bruker Vertex 80v Fourier Transform spectrometer, and occurred close to 8 μm . This agrees with data presented for recently fabricated purified GLS compositions [23], where the absorption coefficient at 7.8 μm was $\alpha \approx 1 \text{ cm}^{-1}$ (for comparison, for IG2, $\alpha = 0.02 \text{ cm}^{-1}$ at the same wavelength). This will also contribute to the high propagation losses observed. These results promote the use of IG2 as an alternative to GLS for applications in the 8–12 μm spectral band, where GLS becomes redundant.

Conclusion

In this work, the demonstration and characterization of mid-IR waveguides realized by ultra-fast laser inscription in IG2 chalcogenide glass has been reported. Waveguides in IG2, exploring the ULI parameter space, were produced and subsequently characterized in terms of mode profile and transmission using a QCL emitting at 7.8 μm . For comparison, waveguides inscribed in GLS were also characterized, since this material has already been well established and characterized as far as mid-IR ULI waveguides are concerned.

To put the work into context, and estimate key inscription parameters, the inscribed structures were modelled. Two different indirect methods were employed to estimate the refractive index variation induced by ULI: the use of mode field diameter dependence on waveguide dimensions; and the refractive index modification threshold allowing the support of higher order modes. The latter method was shown to be the more accurate approach. However, both methods returned consistent estimates of Δn ranging from 0.010 to 0.015 for inscription pulse energies of 10–16 nJ in the case of IG2, and $\Delta n < 0.006$ for inscription energies up to 60 nJ for GLS.

Compared to GLS, IG2 allows larger refractive index contrast, even for lower pulse energy. It was also observed to be more resilient to damage during the inscription process. In addition, the benefits of ease of procurement, and a larger transparency window going deeper towards the long wave infrared, IG2 appears to be an ideal material for ULI waveguides and the development of mid-IR integrated photonic devices.

Immediate follow-on work includes deriving a more robust estimate of the dependence of Δn with inscription pulse energy with use of a larger data set. In addition, more complex structures involving bends and evanescent couplers are currently being produced and will be characterized.

Funding

Science and Technology Facilities Council (STFC) Center for Instrumentation (UK), through Engineering and Physical Sciences Research Council (EPSRC) Centre for Innovative Manufacturing in Laser-based Production Processes (EP/K030884/1), and through STFC Consortium Grant ST/N000625/1.

Acknowledgment

We acknowledge the support of the Precision Development Facility within the Space Science and Technology Department (RAL Space) at the Rutherford Appleton Laboratory, for assistance in design and manufacture of precision components for the waveguide characterization rig.